Acta Geotechnica manuscript No.
(will be inserted by the editor)

Effect of particle friction and polydispersity on the macroscopic stress-strain relations of granular materials

Fatih Göncü · Stefan Luding

Received: date / Accepted: date

Abstract The macroscopic mechanical behavior of granular materials inherently depends on the properties of particles that compose them. Using the Discrete Element Method, the effect of particle contact friction and polydispersity on the macroscopic stress response of 3D sphere packings is studied. The analytical expressions for the pressure, coordination number and fraction of rattlers proposed for isotropically deformed frictionless systems also hold when the interparticle coefficient of friction is finite, however the numerical values of the parameters such as the jamming volume fraction change with varying microscopic contact and particle properties.

The macroscopic response under deviatoric loading is studied with triaxial test simulations. Concerning the shear strength, our results agree with previous studies showing that the deviatoric stress ratio increases with particle coefficient of friction μ starting from a non-zero value for $\mu = 0$ and saturating for large μ. On the other hand, the volumetric strain does

Fatih Göncü · Stefan Luding
Multi Scale Mechanics (MSM), Faculty of Engineering Technology,
University of Twente, PO Box 217, 7500 AE Enschede, The Netherlands
E-mail: f.goncu@utwente.nl

NanoStructured Materials (NSM), ChemTech,
Delft University of Technology, Delft, The Netherlands

not have a monotonic dependence on the particle contact friction. Most notably, maximum compaction is reached at an intermediate value of the coefficient of friction $\mu \approx 0.3$. The effect of polydispersity on the macroscopic stress-strain relationship cannot be studied independent of initial packing conditions. The shear strength increases with polydispersity when the initial volume fraction is fixed, but the effect of polydispersity is much less pronounced when the initial pressure of the packings is fixed. Finally, a simple hypoplastic constitutive model is calibrated with numerical test results following an established procedure to ascertain the relation between particle properties and material coefficients of the macroscopic model. The calibrated model is in good qualitative agreement with simulation results.

Keywords Granular matter · friction · polydispersity · triaxial test · hypoplastic constitutive model

1 Introduction

Understanding the mechanical properties of granular materials and their connection to the microscale particle properties is important for many industrial applications and basic research. Even when grain scale properties such as shape, roughness and elasticity are known it is not straight forward to relate them to the macroscopic constitutive behavior. The main difficulty arises from the discreteness and disorder of granular materials which leads to reorganizations of the inhomogeneous and anisotropic contact and force networks and distributions [1, 2].

In general, two types of approach focusing on different length scales are pursued to model the mechanical behavior of granular materials. Micro-mechanical [3] models consider individual particles and their interactions with the surrounding, for example, by specifying contact force laws and inter-particle friction. Although this is analytically tractable

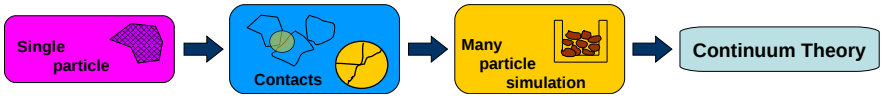

Fig. 1: Approach to study the macroscopic continuum behavior of granular materials with discrete particle methods.

for a limited number of particles, it is usually implemented numerically in discrete particle methods [4] for useful results. Large scale phenomena and industrial applications of granular materials involve countless particles. Even with the most advanced computational technology of today it is not possible to simulate a nature-scale realistic system following this approach.

An alternative is to assume a granular medium as a continuum and apply the principles of continuum mechanics to obtain macroscopic field variables. Generally numerical methods implementing this approach require comparatively less computational resources. However, besides the lower resolution one has to sacrifice many features of granular materials readily implemented in discrete methods, such as re-structuring, geometric non-linearity due to discreteness, explicit control over particle properties etc. Instead an empirical constitutive model has to be defined typically based on phenomenological observations of the relation between stress and strain. Although, micromechanical parameters are introduced [5–7] to enhance the models, the main drawback of the continuum approach remains its lack of connection with the microscopic behavior and properties of the constituent particles.

Despite their disadvantage in large scale simulations, particle methods can be used to understand the macroscopic constitutive behavior and develop models of granular materials, as illustrated in Fig. 1. In particular, the possibility to selectively control properties at the particle level enables to determine their role in the constitutive behavior. In this paper we study the effect of particle polydispersity and friction on the macroscopic stress-strain relations of sphere packings. For this, we systematically vary the size ratio and the coefficient

of friction of the particles in discrete element method (DEM) simulations. The results of triaxial test simulations are then used to calibrate the material coefficients of a hypoplastic constitutive model to determine their relation with particle properties.

The manuscript is organized as follows: In section 2 we describe the general numerical setup for sample preparation and parameters used in simulations. Next in section 3 we present results of isotropic deformation simulations of frictional packings and compare the evolution of the pressure with previously studied frictionless packings with varying polydispersity. Section 4 introduces the hypoplastic constitutive model. In Section 5 we present the results of triaxial test simulations and discuss the macro behavior before we calibrate the hypoplastic model for different contact coefficients of friction and particle polydispersities.

2 Simulation setup

The motion of N spherical particles with uniformly distributed radii between $r_{\min}$ and $r_{\max}$ was simulated using the Discrete Element Method (DEM) [4]. Linear spring–dashpot contact force laws as function of the overlaps are used to model the interaction of particles in the normal and tangential directions [8]. Friction was modelled according to the Coulomb law involving a sliding friction. Gravity was neglected during all simulations and an artificial background dissipation proportional to the translational and rotational velocities was included to damp the slow, large wavelength dynamics. Numerical values of the parameters used in our simulations are presented in Table 1.

Cuboid samples were prepared from random granular gases with initial volume fraction $\nu_{\text{gas}} = 0.3$ with prescribed polydispersities, where the volume fraction ν is the ratio of total volume of particles and system volume. The packings were compressed isotropically by moving periodic boundaries until the volume fraction reached selected value for

Parameter	Value	Description	Dimensionless values
N	9261 [–]	Number of particles	9261
$\langle r \rangle$	1 [mm]	Average radius	1
w	1−5 [–]	Polydispersity parameter $w = r_{\max}/r_{\min}$	1−5
ρ	2000 [kg/m^3]	Density	2000
k_n	10^4 [kg/s^2]	Stiffness–normal spring	10^5
k_t	2×10^3 [kg/s^2]	Stiffness–tangential spring	2×10^4
μ	0−100 [–]	Coefficient of friction	0−100
γ_n	10^{-2} [kg/s]	Viscous dissipation–normal direction	1000
γ_t	2×10^{-3} [kg/s]	Viscous dissipation–tangential direction	200
γ_{tr}	10^{-4} [kg/s]	Background damping–Translation	10
γ_{rot}	2×10^{-5} [kg/s]	Background damping–Rotation	2
τ_c	64 [μs]	Duration of a collision for two average size particles	0.64

Table 1: Summary and numerical values of particle parameters. The dimensionless values used in DEM simulations are such that the unit of length is $x_u = 10^{-3}$ m, the unit of density is $\rho_u = 1\,\mathrm{kg\,m^{-3}}$, which leads to the unit of mass of $m_u = 10^{-9}$ kg, and the set is completed by the unit of time $t_u = 10^{-4}$ s= 0.1 ms. Stress values from the simulations are thus translated to dimensional units by multiplication with $m_u/(x_u t_u^2) = 10^2\,\mathrm{kg/(ms^2)}$.

the subsequent isotropic compression and unloading cycle. The boundaries were displaced using a cosine wave function to avoid shocks. The systems were then relaxed at constant volume fraction to dissipate most of the remaining kinetic energy. Fig. 2 illustrates sample preparation and a typical simulation of an isotropic deformation cycle.

It was previously observed [9, 10] that friction has an important effect on the structure and geometry of loose packings generated by compressing random granular gases. The preparation history, which can influence the mechanical behavior of granular packings at later stages, is *not* our aim in this study. However, when studying the effect of friction, we did not entirely disregard it by preparing frictionless samples. Instead, to minimize the effect of friction during the preparation procedure, very soft tangential springs, i.e. $k_t/k_n = 0.01$ were used. This has no visible consequences for the samples prepared below the jamming

density. However, as it will be shown in Sec. 5.1, even with soft tangential springs particle friction has noticeable repercussion, e.g. on pressure, at higher densities. Note that in actual simulations (after the preparation step) the tangential spring stiffness is set to $k_t = k_n/5$.

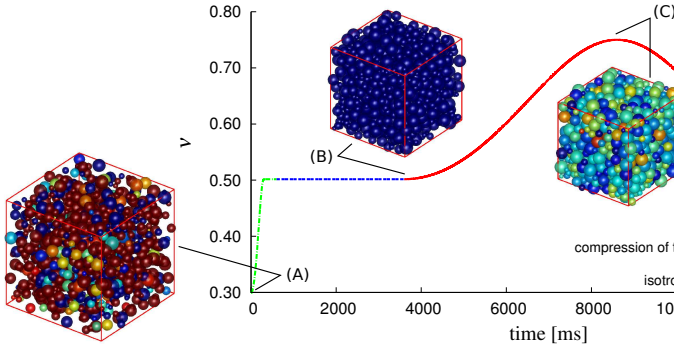

Fig. 2: Preparation of a sample and isotropic compression-expansion cycle. The initial random granular gas (A) is compressed until the volume fraction reaches the desired value. It is then relaxed at constant volume and used as the initial packing (B) for subsequent simulations. The color of particles indicates their average overlap. Large (artificial) overlaps are present in the initial random gas (red particles) whereas in the relaxed packing (blue) particles practically do not touch. The variation in color in the static packing (C) at maximum density is due to well known force-chain inhomogeneity. The data presented subsequently in section 3 corresponds to the branch (C)-(D).

3 Isotropic deformations: Evolution of pressure

Experimental [11] and numerical investigations [9, 12] in 2 and 3 dimensions have shown that pressure along with other quantities such as the coordination number are evolving as a power law of volume fraction in the vicinity of jamming. In our earlier work [13] we derived an analytical expression of the dimensionless pressure $p = \frac{2\langle r\rangle}{3k_n}\mathrm{tr}(\sigma)$ for packings of frictionless polydisperse particles which is applicable to a wide range of volume fractions above jamming:

$$p = \lambda \frac{\nu Z}{\nu_c}(-\varepsilon_v)\left[1-\gamma_p(-\varepsilon_v)\right], \tag{1}$$

where Z is the coordination number, ν_c is the critical (jamming) volume fraction where the pressure drops to zero during unloading, $\varepsilon_v = \ln(\nu_c/\nu)$ is the compressive volumetric strain applied to the packing, and λ and γ_p are fit parameters, (see [13] for an interpretation of their physical meaning). The derivation was based on the assumptions that the compacity (contacts per surface area) of particles is independent of their size and they deform affinely in the assembly, see also [14]. The scaling of the dimensionless pressure by the ratio of inverse contact density and the critical volume fraction, $p^* = \frac{\nu_c}{\nu Z} p$, indicates that the effect of the polydispersity on pressure is characterized by these quantities. This was confirmed in simulations [13] for polydispersities up to $w = 3$. Furthermore, we tested the validity of the power law for the coordination number ignoring rattlers, i.e. frictionless particles having less than 4 contacts, at high volume fractions:

$$Z^*(\nu) = Z_0 + Z_1 \left(\frac{\nu}{\nu_c} - 1 \right)^{\alpha}, \tag{2}$$

where Z_0 is the critical coordination number at jamming, which is equal to 6 in the isostatic limit for frictionless particles, and Z_1 and α are fit parameters. The classical coordination number Z (taking rattlers into account) is related to Z^* through $Z = Z^*(1 - \phi_r)$, where ϕ_r is the fraction of rattlers, which we observed to decay [13] exponentially as a function of the volume fraction:

$$\phi_r(\nu) = \phi_c \exp\left[-\phi_\nu \left(\frac{\nu}{\nu_c} - 1 \right) \right], \tag{3}$$

where ϕ_c is the fraction of rattlers at jamming and ϕ_ν is the rate of decay with density above ν_c. In summary, combining Eqs. (2) and (3) one can express the dimensionless pressure (1) merely as a function of the volume fraction [13].

Next we study numerically the evolution of pressure in isotropically deformed assemblies with varying particle coefficient of friction and fixed polydispersity $w = 1.5$. Samples

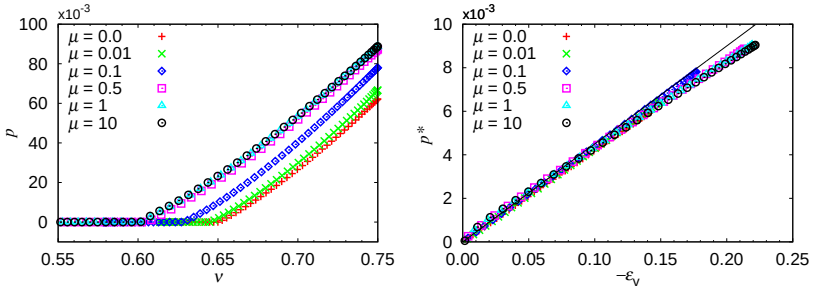

(a) (b)

Fig. 3: (a) Non-dimensional pressure p as function of the volume fraction and (b) scaled pressure $p^* = p\nu_c/(\nu Z)$ as function of volumetric strain. The points represent simulation data, while the line in (b) is $p^* = -\varepsilon_v \lambda$ with $\lambda = 0.045$.

were prepared, as described in Section 2, at a few percent, i.e. $\Delta\nu = \nu_c - \nu_0 \approx 0.05$, below the estimated jamming volume fractions [15]. The packings were compressed up to $\nu = 0.75$ and decompressed back to their initial density by imposing a cosine shape displacement on the periodic boundaries. We applied the strains at very low rates in order to approach the quasi-static limit. The rate dependence was studied in Ref. [13]. The maximum average compression rate [1] was $6.33 \times 10^{-6}\ \tau_c^{-1}$.

Figure 3a shows the dimensionless pressures of isotropically expanding [2] packings as a function of volume fraction for different levels of particle friction. The pressure at a given volume fraction increases with the coefficient of friction and the volume fraction of vanishing pressure ν_c decreases with friction [9, 10, 15–17]. However the effect of particle friction on pressure seems to be limited as the lowest value of ν_c saturates around a minimum of ~ 0.60 when μ tends to infinity. Numerical values of ν_c are given in Table 2 and the procedure to obtain them will be discussed below. In moderately frictionless polydisperse

[1] The average compression (expansion) rate is computed as $\frac{\Delta V/V_0}{T_c} = \frac{\nu/\nu_0 - 1}{T_c}$ where T_c is the half period of the cosine wave displacement function.

[2] The data is not shown during compression but during decompression because of artificial dynamical effects in the former, see [13] for a detailed discussion.

packings ν_c is observed to increase with w [13, 18], whereas it is decreasing with friction and rolling resistance [15] as consistent with the present data.

The scaled dimensionless pressure is shown in Figure 3b. In contrast to previously studied frictionless polydisperse systems, there is *not* a perfect collapse of the data on a single line, which indicates that the effect of particle friction on pressure cannot be assessed solely by the contact density and critical volume fraction. However, the quasi-linear dependence on strain is similar. Nevertheless somewhat stronger non-linearity at low strains is noticeable for large coefficients of friction which causes the quality of the fit of Eq. (1) to deteriorate for $\nu \approx \nu_c$.

For completeness we also show in Figures 4a and 4b the coordination number Z^* and fraction of rattlers ϕ_r as a function of volume fraction. The critical coordination number $Z_0 = 5.95$ of the frictionless packing obtained from the fit of Eq. (2) is very close to the theoretically predicted isostatic limit 6. As the particle friction increases Z_0 decreases towards 4 (see Table 2). The exponential decay function is underestimating the fraction of rattlers close to unjamming for large particle friction. This is due to the fact that the criterion of having less than 4 contacts for identifying rattlers is not accurate for frictional particles. About 2.7 % of the particles are rattlers in the frictionless packing (see Table 2). Earlier studies have reported about 2 % rattlers for frictionless monodisperse systems [9, 12]. The slightly higher value in our simulation is due to the small amount of polydispersity ($w = 1.5$) present. However, in more polydisperse systems ($w = 3$) we have measured a considerably higher percentage of rattlers i.e. $\phi_c \approx 15$ % [13]. We also observe that the decay rate is decreasing as the particle coefficient of friction is increasing, which is in line with the expectation that frictional packings most likely to contain a higher number of rattlers.

The analytical expressions (1), (2) and (3) of the pressure, coordination number and fraction of rattlers respectively, all depend sensibly on the critical volume fraction ν_c. Therefore,

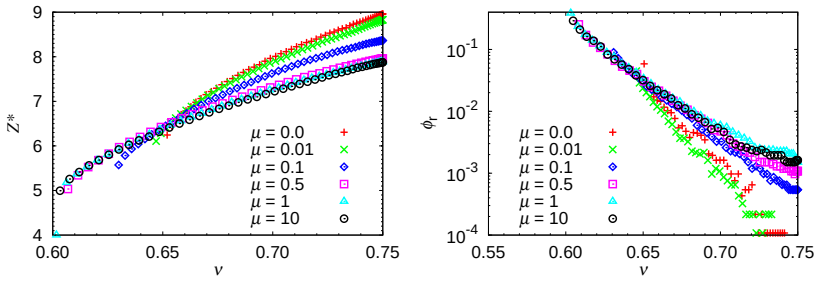

(a) (b)

Fig. 4: (a) Coordination number excluding rattlers as function of the volume fraction for different particle friction coefficients. (b) fraction of rattlers i.e., particles with less than 4 contacts for different particle friction coefficients.

it cannot be obtained from the fits as a parameter but must be determined independently. During isotropic decompression, ν_c corresponds to the volume fraction where the pressure vanishes and the system looses its mechanical stability [9, 12]. We expressed this with an energy criterion which states that ν_c is the first point on the volume fraction axis where the average elastic energy per particle drops below 10^{-5} μJ. Note that a precise definition of ν_c does not exist and other authors [9, 12, 13, 19] have used similar criteria to quantify ν_c. The numerical values of the fit parameters based on two alternative ways to determine ν_c are given in Table 2.

We studied the evolution of pressure in isotropically deformed frictional packings prepared with soft tangential springs $k_t/k_n = 0.01$. Interestingly, the equations for pressure, coordination number and rattlers originally proposed for frictionless systems also hold for finite particle coefficient of friction. We note that, the prefactor λ is practically constant thus independent of μ, which to our knowledge, has not been predicted theoretically before.

μ	ν_c	Z_0	Z_1	α	ϕ_c	ϕ_ν	λ	γ_p
	Energy							
0.0	0.650	5.95	8.66	0.564	0.027	40.84	0.0426	0.069
0.01	0.645	5.85	8.67	0.589	0.031	44.74	0.0425	-0.108
0.1	0.628	5.24	7.86	0.555	0.087	30.53	0.0441	0.000
0.5	0.605	4.79	7.09	0.556	0.165	22.94	0.0457	0.453
1	0.602	4.74	7.10	0.573	0.160	20.34	0.0458	0.467
10	0.600	4.68	7.21	0.583	0.179	21.73	0.0458	0.515
	Extrapolation							
0.0	0.650	5.98	8.71	0.572	0.024	37.71	0.0430	0.114
0.01	0.645	5.88	8.72	0.598	0.031	44.76	0.0428	-0.066
0.1	0.628	5.29	7.89	0.564	0.086	30.54	0.0446	0.045
0.5	0.605	4.77	7.09	0.553	0.166	22.93	0.0455	0.439
1	0.601	4.68	7.09	0.562	0.170	20.66	0.0450	0.417
10	0.599	4.60	7.21	0.569	0.191	21.90	0.0446	0.440

Table 2: Summary of the parameters appearing in the equations (2), (3) and (1) for the coordination number $Z^*(\nu)$, fraction of rattlers $\phi_r(\nu)$ and dimensionless pressure $p(\nu)$, respectively. The numerical values of all parameters except ν_c are obtained from fits to simulation data. The critical volume fractions are extracted from the dimensionless pressure data during decompression where the average potential energy per particle drops below 10^{-5} μJ. (Energy) or alternatively, by extrapolating the pressure in Eq. (1), excluding the data points closest to and below ν_c (Extrapolation).

4 Hypoplastic constitutive model

As pointed out earlier, a continuum mechanical description of granular materials disregards their discrete nature and focuses on the macroscopic relation between stress and strain. Constitutive models for the plastic deformation of granular materials have been typically developed in the framework of elasto-plasticity [20] which requires a yield surface defined in the principal stress space and a flow rule to determine the direction of plastic strain. More recently, enhanced models based on higher order gradients of the strain tensor and micropolar Cosserat type models with additional degrees of freedom have been developed, to address the microstructural effects, see e.g. [21, 22] among others. Alternative formulations based on rate equations were proposed as hypoplastic type of models [23]. It is claimed that they lead to simpler formulations without explicit recourse to a yield surface or flow rule, using however the concept of limit states, and are able to capture basic features of granular

materials. We choose a simple variant of these models for subsequent analysis because of their aforementioned advantages and the possibility to calibrate the model with a single triaxial test. The goal is then to understand the relation between the macro-parameters and the micro-properties.

A hypoplastic constitutive model $\mathring{\mathbf{T}} = \mathbf{H}(\mathbf{T},\mathbf{D})$ relates [23–25] the rate of the stress tensor $\mathring{\mathbf{T}}$ to itself and the rate of deformation tensor $\mathbf{D}$, where $\mathring{\square}$ denotes the objective Jaumann rate. Basic ingredients of hypoplasticity are (i) rate independence, (ii) homogeneity in stress and (iii) objectivity, which is a requirement for all constitutive models. One of the simplest hypoplastic constitutive models, which satisfies these conditions has the form [24]:

$$\mathring{\mathbf{T}} = C_1\,\mathrm{tr}(\mathbf{T})\mathbf{D} + C_2\frac{\mathrm{tr}(\mathbf{TD})\mathbf{T}}{\mathrm{tr}\,\mathbf{T}} + \left(C_3\frac{\mathbf{T}^2}{\mathrm{tr}\,\mathbf{T}} + C_4\frac{\mathbf{T}^{*2}}{\mathrm{tr}\,\mathbf{T}}\right)||\mathbf{D}||, \tag{4}$$

where $\mathbf{T}^*$ is the deviatoric part of the stress tensor. $||\mathbf{D}|| = \sqrt{\mathrm{tr}\,\mathbf{D}^2}$ is the norm of the rate of deformation tensor and C_1, C_2, C_3 and C_4 are material coefficients. The first two terms of Eq. (4) express the linear elastic part of the model. A decomposition of the stress and strain tensors into isotropic and deviatoric parts shows that under simple biaxial conditions the bulk modulus and the anisotropy can be directly related to the coefficients C_1 and C_2 [26].

In order to predict the mechanical behavior of a specific material, a constitutive model needs to be adapted by providing a suitable set of material coefficients which are usually obtained by calibrating the model with experimental data. Results of a single triaxial test are sufficient to calibrate the hypoplastic constitutive model given in Eq. (4). The procedure [24, 25] which consists of solving a linear system of equations to find the numerical values of the material coefficients C_1, C_2, C_3 and C_4 is summarized in Appendix A.

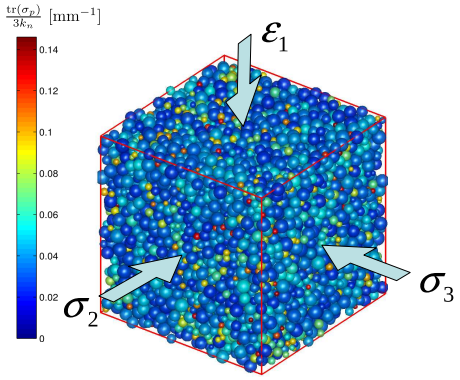

Fig. 5: Triaxial test simulated with DEM. The boundary conditions are such that the pressure on the side walls $\sigma_2 = \sigma_3$ is kept constant and the strain on top is increased monotonically. The color indicates the pressure of particles normalized by the normal contact stiffness k_n. The pressure is computed according to $\frac{1}{3}\,\mathrm{tr}(\sigma_p) = \frac{k_n}{3V_p}\sum \delta(r_p - \delta/2)$ where V_p is the volume of the particle and δ is its overlap with neighbors which is averaged over all its contacts.

5 The triaxial test

The triaxial test is a standard laboratory test procedure widely used to measure mechanical properties of soils [25] and other granular materials. The classical experiment typically consists of compressing a cylindrical specimen wrapped in a membrane in axial direction while keeping the lateral stress constant by means of hydrostatic pressure. We have implemented the triaxial test in DEM simulations for a cubic geometry with periodic boundary conditions in order to avoid wall effects. Similar to the experimental setup, the pressure on the lateral walls (i.e. periodic boundaries) is kept constant while applying a monotonically increasing strain in the third direction. Figure 5 illustrates the numerical simulation setup. The average stress of the packing is measured according to the procedure described in [13, 27, 28].

In the following we perform triaxial test simulations with frictional and polydisperse packings and calibrate the hypoplastic constitutive model with the numerical data to understand the relation between material coefficients and particle properties. The initial packings

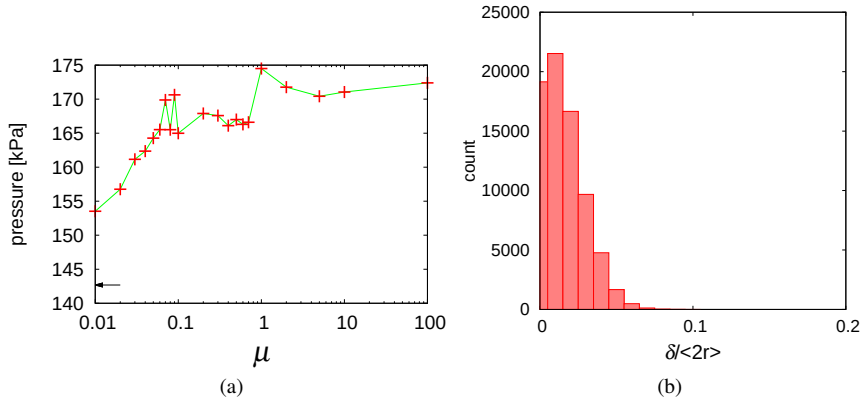

Fig. 6: (a) Average pressure of the packings as function of particle coefficient of friction for $\nu_0 = 0.70$ and $w = 1.5$. The pressure of the frictionless packing is indicated by the arrow. The symbols are data, the lines only a guide to the eye. (b) Histogram of normalized particle overlaps in the packing with $\mu = 1$.

were prepared as described in Sec. 2 with different particle friction and polydispersities at volume fractions $\nu_0 > \nu_c$.

5.1 Friction

Figure 6a shows the pressure of the initial samples prepared at $\nu_0 = 0.70$ from a granular gas with $w = 1.5$ as a function of the particle friction. In accordance with the observations in Section 3 the pressure increases with friction and saturates at very high values of μ. However, note that we have used very soft tangential springs ($k_t = 10^2$ [kg/s^2], $k_t/k_n = 0.01$) to reduce the effect of friction during the preparation. Nevertheless, it has still a noticeable effect on the pressure build-up during initial compression as the difference of pressure for $\mu = 0$ and $\mu = 0.01$ is about 8 % and, for $\mu = 0.01$ and $\mu = 100$ is about 10 %.

Since the density and thus the pressure is considerable, we have checked the distribution of particle overlaps in the packings. Fig. 6b shows the histogram of overlaps normalized by the average particle diameter in the packing with highest pressure ($\mu = 1$). Although some

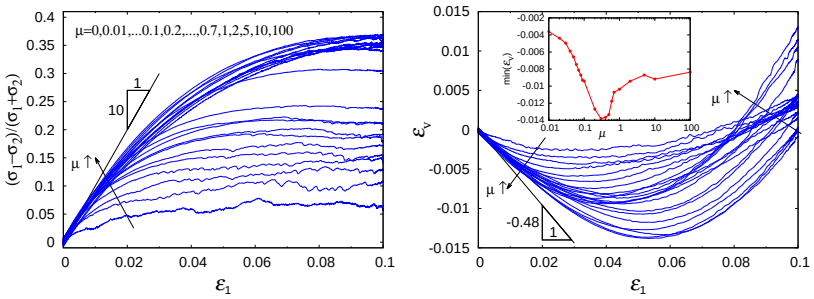

Fig. 7: Results of DEM triaxial test simulations with different particle coefficients of friction. (a) Deviatoric stress ratio, (b) volumetric strain as a function of axial strain. The inset shows the minimum volumetric strain, i.e. the maximal compression as a function of particle friction.

particles have large overlaps the percentage is small. More than 96% of the overlaps are smaller than 5% of average particle diameter. Therefore, it is expected that this will not have a significant effect on the qualitative behavior observed hereafter.

The results of DEM triaxial test simulations are shown in Figures 7a and 7b for the evolution of deviatoric stress ratio and the volumetric strain. Fluctuations and non-zero values at the initial configurations are due to the stress control algorithm which cannot strictly enforce the prescribed lateral stress (taken as the average of σ_{xx}, σ_{yy} and σ_{zz} after isotropic compression). For the strain levels applied in our simulations softening after the maximum stress is not observed. However, in a few simulations up to 20 % axial strain the packings with higher particle friction exhibited some softening. In any case the strain levels were not enough to reach the critical state where the stress and volumetric strain have stationary values [29]. The inset of Figure 7b shows that the maximum compaction of the packings does not have a linear relationship with the particle friction. It increases with friction and reaches an extremum at $\mu = 0.3$, then decreases and stagnates around $\varepsilon_v \approx -0.01$ for $\mu \geq 1$. The axial strains where the maximum compaction is achieved show a similar trend.

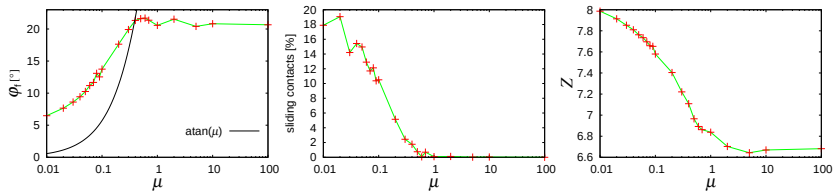

(a) (b) (c)

Fig. 8: (a) Macroscopic angle of friction, (b) percentage of sliding contacts and (c) coordination number at the peak stress plotted as a function of particle coefficient of friction.

Figure 8a shows the macroscopic angle of friction defined by $\varphi_f = \arcsin((\sigma_1 - \sigma_2)/(\sigma_1 + \sigma_2))_{\max}$ as a function of the particle coefficient of friction. It is rapidly increasing and saturates around 21 degrees for $\mu \geq 1$. The percentage of sliding contacts at the peak stress is given in Fig. 8b. For large particle friction, i.e. $\mu \geq 1$, less than 1 % of the contacts are sliding. This is in agreement with previous experiments [30] and simulations [31–33]. As shown in Fig. 8c the average number of contacts at the peak stress is also decreasing when particle friction is increased. The average contact force is higher in packings with large particle friction because of the lower coordination number and higher macroscopic stress carried by the structure. We also observe that the coordination number of the frictionless packing is practically constant during loading whereas for high friction it decreases linearly with axial strain (data not shown). Finally we note that the macroscopic friction angle is smaller than the contact friction angle when $\mu > 0.4$. The numerical values of macroscopic friction angles, percentage of sliding contacts and coordination number are listed in Table 3.

Previous studies have explored the mechanism behind the effect of particle friction on the macroscopic behavior of granular materials[31–33]. It was shown that the contact force network can be divided into strong and weak forces and particle friction increases the contribution of strong contact forces to major principal stress and decreases their contribution to minor principal stress which leads to increasing deviatoric stress [33]. Furthermore, the finite

shear strength of frictionless particles can be attributed to interlocking and stress anisotropy which is present even in initially isotropic packings. Saturation of the macroscopic friction angle at large particle friction is due to rolling of particles as it was shown that preventing particle rotation leads to increasing macroscopic friction [31]. Below is a summary of our observations of the effect of particle friction which are consistent with earlier studies in 2D (see Figs. 26 and 27 in Ref. [34] and references therein) and in 3D (see eg. [16, 31, 33]):

1. Stronger particle friction leads to smaller jamming densities
2. Finite macroscopic friction is measured even for $\mu = 0$
3. Macroscopic friction saturates for $\mu \gtrapprox 0.3$
4. Macroscopic friction does not match particle friction

The effect of particle friction on the peak/softening behavior goes beyond the scope of this paper.

We now compare the results of the triaxial tests from DEM and with the calibrated hypoplastic model. Figure 9a shows the deviatoric stress ratio and volumetric strain as a function of axial strain for small and large particle friction. The calibrated hypoplastic model (see Appendix A) captures the stress-strain relationship relatively well, however fails to approximate the broad dip in the volumetric strain of the systems with small particle friction. Another disagreement between the model and DEM simulations is the longer linear range during initial loading which leads to higher stiffness and compactancy. Consequently, the model systematically underestimates the axial strains where the packing starts to dilate. Figure 9b shows the relation between the particle coefficient of friction μ and the model coefficients C_1, C_2, C_3 and C_4 obtained from the calibration of the model with DEM simulation data (see Table 3 for numerical values). Although the model results are not in perfect agreement with DEM data we can make a few observations. First, the numerical values of all

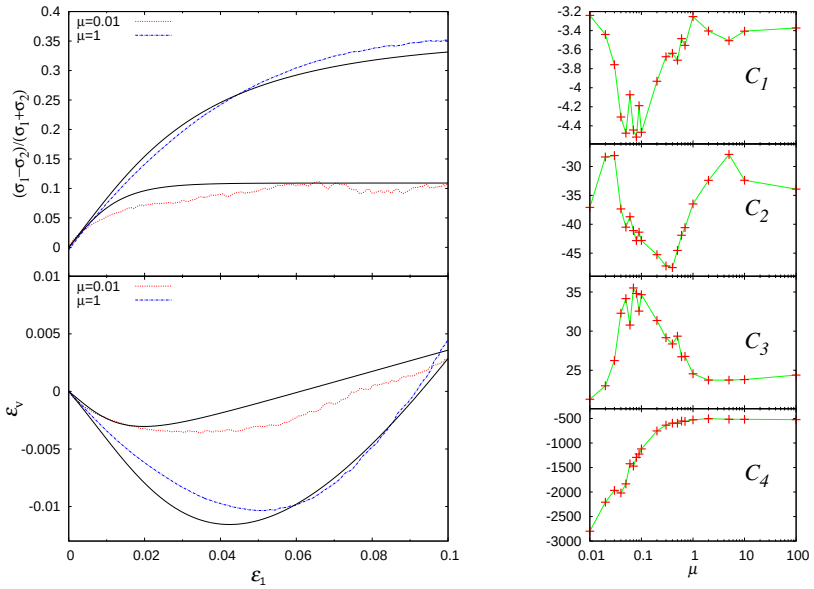

(a) (b)

Fig. 9: (a) Comparison of the triaxial test simulation results of DEM (dashed and dash-dotted lines) and the calibrated hypoplastic constitutive model (solid lines) for $\mu = 0.01$ and 1. (b) Evolution of the material coefficients as function of particle friction.

coefficients seem to saturate at high coefficients of friction i.e. for $\mu > 1$. This is in line with the previously observed limited effect of particle friction on the macroscopic stress-strain relationship for large μ in Fig. 7. Next, C_2 reaches its minimum value (maximal magnitude) at $\mu = 0.3$ which coincides with the coefficient of friction of the packing which is most compacted. We also note that C_1 and C_3 have extremal values at $\mu \simeq 0.09$ but we were not able to relate it to any of the microscopic quantities studied here. Finally, the coefficient C_4, which is multiplying the last term of the hypoplastic model in Eq. (4), with the deviatoric stress is strongly correlated with the macroscopic angle of friction.

The relatively small magnitude of C_3 compared to C_4 suggests that the third term in Eq. (4) can be neglected. Nevertheless, imposing $C_3 = 0$ during the calibration procedure significantly affects other coefficients which in turn leads to large discrepancies between the

model and DEM results. Furthermore, as discussed in Ref. [24] the hypoplastic model considered here cannot reproduce softening and the critical state, which limits the applicability of the model to small and moderate strains.

5.2 Polydispersity

An important property of natural granular materials is polydispersity i.e. the size disorder of the grains. In this subsection we study the effect of size distribution on the macroscopic stress-strain relationship of granular materials with DEM simulations of the triaxial test. In contrast to subsection 5.1, initial samples were prepared at $\nu_0 = 0.70$ by isotropic com-

μ	p_0 [kPa]	ϕ_f [°]	sliding contacts [%]	Z	C_1	C_2	C_3	C_4
0.0	142.6	4.00	0	8.01	-1.51	-15.81	8.88	-2916.24
0.01	153.5	6.26	17.8	7.98	-3.20	-36.96	20.80	-2763.10
0.02	156.7	7.42	19.0	7.91	-3.39	-28.04	22.61	-2173.83
0.03	161.1	8.40	14.2	7.85	-3.72	-27.86	26.01	-1948.24
0.04	162.3	9.10	15.4	7.80	-4.30	-37.34	32.29	-2019.97
0.05	164.2	9.95	14.9	7.76	-4.49	-40.64	34.33	-1841.77
0.06	165.5	11.04	12.8	7.73	-4.06	-38.62	30.65	-1418.35
0.07	169.8	11.56	11.7	7.69	-4.47	-41.28	35.92	-1484.12
0.08	165.5	12.70	12.1	7.65	-4.55	-43.11	35.12	-1304.17
0.09	170.6	12.55	10.3	7.65	-4.21	-41.60	32.81	-1234.32
0.1	164.9	14.01	10.5	7.57	-4.49	-43.08	34.98	-1129.61
0.2	167.8	17.89	5.1	7.40	-3.95	-45.55	31.64	-758.79
0.3	167.5	20.06	2.4	7.22	-3.68	-47.34	29.21	-637.61
0.4	166.1	21.32	1.7	7.10	-3.64	-47.51	28.30	-594.43
0.5	167	21.53	0.7	6.96	-3.72	-44.63	29.51	-598.60
0.6	166.2	21.57	0.1	6.89	-3.48	-41.84	26.64	-550.80
0.7	166.6	21.27	0.6	6.86	-3.55	-40.61	26.77	-560.43
1	174.5	20.57	0.1	6.83	-3.24	-36.43	24.52	-526.73
2	171.7	21.15	0.1	6.70	-3.40	-32.37	23.68	-502.58
5	170.4	20.26	0.02	6.64	-3.51	-28.02	23.85	-517.91
10	171.0	20.65	0.03	6.66	-3.39	-32.32	23.73	-515.17
100	172.3	20.68	0	6.68	-3.37	-34.01	24.46	-524.89

Table 3: Initial pressures p_0, macroscopic angles of friction ϕ_f, percentage of sliding contacts and coordination number at maximum deviatoric stress and calibrated material coefficients of packings with constant initial volume fraction $\nu_0 = 0.70$ and different particle coefficient of friction.

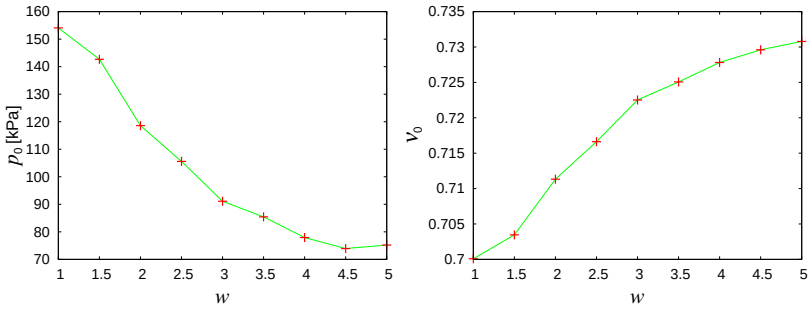

(a) (b)

Fig. 10: (a) Relation between polydispersity w and pressure p in packings with constant volume fraction ($\nu_0 = 0.70$). (b) Relation between polydispersity w and volume fraction ν in packings with constant pressure fraction ($p_0 = 154.1$ kPa).

pression and relaxation of a *frictionless* granular gas. Figure 10a shows the pressure of the samples as a function of the size ratio $w = r_{\max}/r_{\min}$. The results confirm previous studies which have shown that the pressure of frictionless packings at a constant volume fraction decreases with polydispersity [13, 18]. The dependence of the mechanical behavior of granular materials on the initial density and stress level has long been recognized in soil mechanics [24, 35, 36]. The variation of the volume fraction as function of the polydispersity is shown in Fig. 10b for another set of initial samples prepared (again without friction) at constant pressure ($p_0 = 154.1$ kPa). As expected denser packings are needed to achieve a certain level of pressure with more polydisperse particles.

After the frictionless preparation procedure, the coefficient of friction was set to $\mu = 0.4$ for all polydispersities during the triaxial test simulations. Deviatoric stress ratio and volumetric strain as a function of axial strain are shown in Figures 11 and 12 for the constant initial volume fraction and constant initial pressure conditions, respectively. When ν_0 is fixed the shear strength of the packing increases with polydispersity, even though the initial pressure which determines the confining stress $\sigma_2 = \sigma_3 = p_0$ is decreasing with polydispersity, see Fig. 10a. This is in agreement with laboratory experiments of triaxial tests

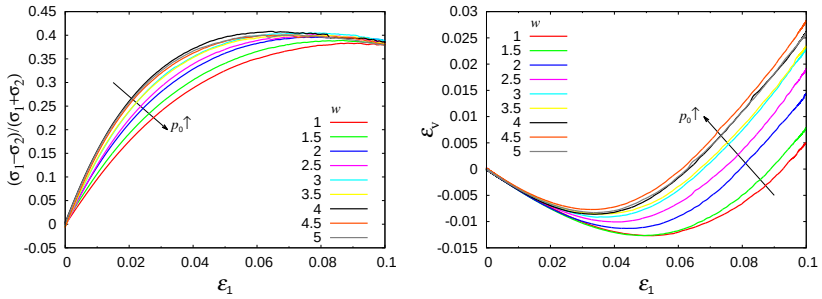

(a) (b)

Fig. 11: Triaxial test simulation results for polydisperse packings of spheres with fixed initial volume fraction $\nu_0 = 0.70$. (a) Deviatoric stress ratio and (b) volumetric strain plotted against axial strain.

performed at different stress levels which indicate that the macroscopic friction angle decreases with confining pressure [36]. However, as illustrated in Fig. 11b, we observe that the "compactancy" angle $\psi_0 = \arctan(\dot{\varepsilon}_v/\dot{\varepsilon}_1)_{\varepsilon_1=0}$ at the initial loading and the dilatancy angle $\psi = \arctan(\dot{\varepsilon}_v/\dot{\varepsilon}_1)_{\varepsilon_1|\sigma_1=\sigma_{1,\max}}$ at peak stress are practically independent of polydispersity and thus of pressure. The average values are $\psi_0 \approx -21.4^\circ$ and $\psi \approx 34.8^\circ$.

The results of the triaxial test simulations for the packings prepared at constant pressure are shown in Figure 12. The effect of polydispersity (and that of the initial volume fraction indirectly) is significantly less visible compared to the case of fixed initial volume fraction. Nevertheless, while the deviatoric stress is not much affected, see Fig. 11a, the maximum compaction slightly increases with polydispersity as shown in Fig. 12b. Tables 4 and 5 list the macroscopic angles of friction, the compactancy and dilatancy angles and the calibrated material coefficients of the hypoplastic model for the constant initial volume fraction and constant pressure cases, respectively. Figure 13 illustrates the material coefficients scaled with the values corresponding to the monodisperse packing. Remarkably the dependence of all coefficients on polydispersity is the same. When the initial volume fraction is fixed they increase with polydispersity (pressure). On the other hand, the coefficients do not show

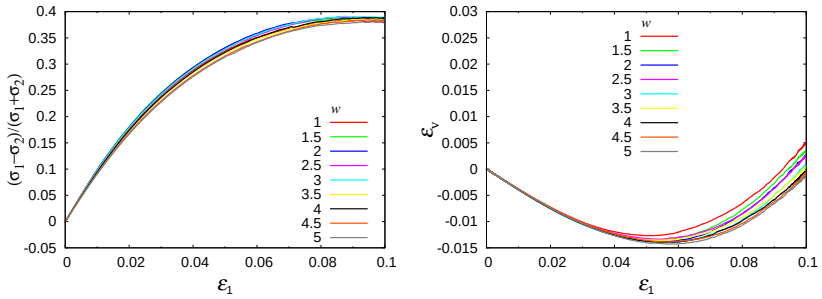

(a) (b)

Fig. 12: Triaxial test simulation results for polydisperse packings of spheres with fixed initial pressure (constant confining stress) $p_0 = 154.1$ kPa. (a) Deviatoric stress ratio, (b) volumetric strain vs. axial strain.

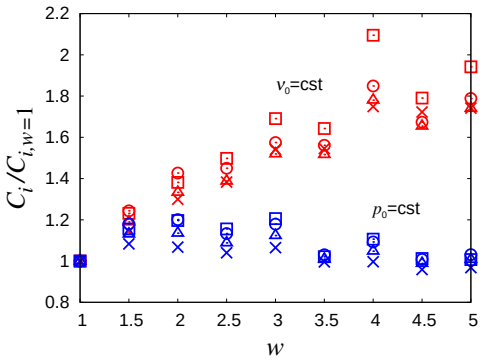

Fig. 13: Material coefficients C_1 ($\times$), C_2 ($\boxdot$), C_3 ($\odot$) and C_4 ($\triangle$) of the calibrated hypoplastic constitutive model normalized with the values obtained for the monodisperse packing $w = 1$. Red and blue symbols correspond to the constant initial volume fraction and pressure cases, respectively.

much variation when the initial pressure is fixed. The effect of different polydispersity is studied in more detail in Refs. [14, 18].

6 Summary and conclusions

We studied the effect of particle friction and polydispersity on the macroscopic mechanical behavior of sphere packings using the discrete element method. Our results support previ-

ous observations on the effect of particle friction in isotropically deformed systems, i.e. the pressure at a given volume fraction decreases with friction and saturates at large values. We also confirm that the critical volume fraction ν_c below which the packing has no mechanical stability decreases with friction. The scaling of the dimensionless pressure by the ratio of inverse contact number density and the critical volume fraction found for frictionless polydisperse packings also applies — although less perfectly, close to ν_c — for strong friction.

The response of the packings to anisotropic deformations was measured with triaxial tests. An increase in particle friction leads to higher macroscopic friction angles, however the shear strength is bounded and does not increase further for $\mu \geq 1$. The effect of particle friction on the evolution of volumetric strain is more subtle. The angle of compactancy decreases with friction, however, the maximum level of compaction is attained by the packing with $\mu = 0.3$. The axial strain of maximum compaction does not correspond to the strain of maximum stress and displays a non monotonic behavior as function of particle friction. Other microscopic quantities such as the fraction of sliding contacts and the coordination number decrease with increasing friction.

The hypoplastic constitutive model is able to reproduce the basic features of the stress strain relationships of the packings. The quantitative agreement is far from perfect, but qual-

w	p_0 [kPa]	ϕ_f [°]	ψ_0 [°]	ψ [°]	C_1	C_2	C_3	C_4
1	154.1	22.49	-21.18	33.04	-4.04	-52.49	31.83	-635.31
1.5	142.7	22.87	-23.53	32.53	-4.62	-64.63	39.58	-755.70
2	118.6	23.39	-24.33	35.57	-5.25	-72.51	45.42	-846.88
2.5	105.6	23.61	-21.72	35.33	-5.58	-78.61	46.16	-881.38
3	91.1	23.95	-20.30	36.15	-6.22	-88.75	50.12	-965.39
3.5	85.4	23.67	-20.43	36.00	-6.24	-86.22	49.70	-963.43
4	77.9	24.09	-20.03	33.52	-7.06	-109.96	58.86	-1130.95
4.5	73.9	23.67	-19.17	36.46	-6.96	-93.98	53.27	-1050.91
5	75.2	23.67	-20.20	34.20	-7.03	-101.93	56.93	-1105.46

Table 4: Initial pressures p_0, macroscopic angles of friction ϕ_f , compactancy ψ_0 and dilatancy ψ angles and calibrated material coefficients of polydisperse packings with constant initial volume fraction $\nu_0 = 0.70$.

w	ν_0	ϕ_f [°]	ψ_0 [°]	ψ [°]	C_1	C_2	C_3	C_4
1	0.700	22.49	-21.28	33.04	-4.04	-52.57	31.94	-636.66
1.5	0.703	22.71	-23.98	32.18	-4.38	-60.73	37.69	-719.80
2	0.711	22.91	-24.38	31.35	-4.31	-62.90	38.36	-722.66
2.5	0.716	22.92	-23.03	31.48	-4.20	-60.75	36.20	-692.63
3	0.722	23.00	-23.36	31.22	-4.30	-63.39	37.66	-715.27
3.5	0.725	22.69	-22.36	33.19	-4.02	-53.68	32.91	-642.44
4	0.727	22.83	-23.35	31.14	-4.03	-58.15	34.90	-667.14
4.5	0.729	22.55	-22.48	31.57	-3.87	-53.22	32.20	-629.29
5	0.730	22.34	-23.44	31.33	-3.91	-52.94	32.94	-641.60

Table 5: Initial volume fractions ν_0, macroscopic angles of friction ϕ_f, compactancy ψ_0 and dilatancy ψ angles and calibrated material coefficients of polydisperse packings with constant initial initial pressure $p_0 = 154.1$ kPa

itatively all features are captured. However because of its phenomenological origin and the complex interplay of the different deformation modes, it was not possible to uniquely and directly link the coefficients of the model to the microscopic particle properties. However, some conclusions are possible since we systematically calibrated the model with DEM simulations in order to clarify the relation between material constants and particle friction. We observe that the third coefficient is positive, while all others are negative. The fourth coefficient follows a trend similar to the macroscopic angle of friction, while the third coefficient is considerably smaller, but must not be set to zero, i.e., it is important nevertheless. The other coefficients have extremal values at various particle friction coefficients corresponding to those of the packings with maximum compaction and initial confining pressure. Their non-monotonous variation with μ reflects the complex influence of the contact friction on the different macroscopic terms in the hypoplastic constitutive relation in Eq. (4).

The effect of the polydispersity of the packings cannot be studied independent of the volume fraction or the pressure of the initial samples. When the volume fraction is fixed the pressure decreases as function of polydispersity. The opposite is observed for the volume fraction when the initial pressure is fixed. The shear strength increases with polydispersity

for the packings with fixed initial volume fraction. On the other hand, the effect of polydispersity is much less pronounced when the initial pressure is constant.

In conclusion, our results support and confirm previous numerical [31–33] and experimental [36] studies based on biaxial and triaxial deformation tests. However, an important difference is that we have studied relatively dense packings and soft particles (normal stiffness corresponds approximately to PMMA) and a wide range of particle friction including the frictionless case. In our opinion, this leads to interesting behavior such as the reversal of the maximum compaction at $\mu = 0.3$ which was not reported previously to the authors knowledge.

Systematic variation of the simulation parameters allows to understand the effect of micro-scale properties on the macroscopic behavior of granular materials in the spirit of the approach sketched in Fig. 1. However, it is difficult to establish a formal relation between the material parameters of a phenomenological constitutive model and microscopic particle properties. Particle simulations can help to identify microscopic mechanisms relevant at the macroscopic scale and facilitate the development of micromechanically based constitutive models for granular materials. The qualitative agreement between DEM and the hypoplastic constitutive model is very encouraging, but the visible quantitative differences could be a sign that important properties, like the structural anisotropy, are missing. The comparison and calibration with an anisotropic constitutive model [37, 38] is in progress.

Acknowledgements This work has been supported financially by the Delft Center for Computational Science and Engineering. Helpful discussions with V. Magnanimo, N. Kumar, W. Wu and J. Tejchman are appreciated.

A Calibration of the hypoplastic constitutive model

The hypoplastic constitutive model given in Eq. (4) can be calibrated for a specific material with the results of a triaxial test [25].

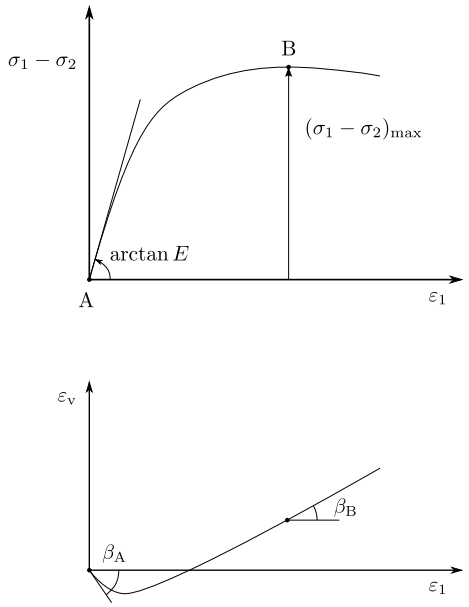

Fig. 14: Schematic representation of a triaxial test result for the calibration of the hypoplastic constitutive model.

Due to the simple geometry of the test setup the stress and strain rate tensors are characterized by their principal components:

$$-\mathbf{T} = \begin{pmatrix} \sigma_1 & 0 & 0 \\ 0 & \sigma_2 & 0 \\ 0 & 0 & \sigma_3 \end{pmatrix} \quad , \quad \mathbf{D} = \begin{pmatrix} \dot{\varepsilon_1} & 0 & 0 \\ 0 & \dot{\varepsilon_2} & 0 \\ 0 & 0 & \dot{\varepsilon_3} \end{pmatrix} , \tag{5}$$

where compressive stresses are positive.

As illustrated in Fig. 14, the values of $(\sigma_1-\sigma_2)_{\max}$, the slope [3] E and the angles β_A and β_B at points A and B can be computed from the test results and are related to $\mathbf{T}$ and $\mathbf{D}$:

$$\beta_{A/B} = \arctan\left(\frac{\dot{\varepsilon}_v}{\dot{\varepsilon}_1}\right)_{A/B} = \arctan\left(\frac{\dot{\varepsilon}_1+2\dot{\varepsilon}_2}{\dot{\varepsilon}_1}\right)_{A/B} = \arctan\left(1+2\frac{\dot{\varepsilon}_2}{\dot{\varepsilon}_1}\right)_{A/B} \tag{6}$$

Since the hypoplastic constitutive model is rate independent the magnitude of the strain rate $|\dot{\varepsilon}_1|$ can be arbitrary. However, the sign of $\dot{\varepsilon}_1$ must be negative due to compression during a conventional triaxial test. Therefore for simplicity $\dot{\varepsilon}_1 = -1$ is chosen so that the strain rate tensor $\mathbf{D}$ at points A and B is:

$$\mathbf{D}_{A/B} = \begin{pmatrix} -1 & 0 & 0 \\ 0 & \frac{1}{2}(1-\tan\beta_{A/B}) & 0 \\ 0 & 0 & \frac{1}{2}(1-\tan\beta_{A/B}) \end{pmatrix}. \tag{7}$$

The stress tensor $\mathbf{T}$ at points A and B is known:

$$-\mathbf{T}_A = \begin{pmatrix} \sigma_2 & 0 & 0 \\ 0 & \sigma_2 & 0 \\ 0 & 0 & \sigma_2 \end{pmatrix} \quad \text{and} \quad -\mathbf{T}_B = \begin{pmatrix} \sigma_2-(\sigma_1-\sigma_2)_{\max} & 0 & 0 \\ 0 & \sigma_2 & 0 \\ 0 & 0 & \sigma_2 \end{pmatrix}, \tag{8}$$

and the stress rates are given by:

$$\dot{\mathbf{T}}_A = \begin{pmatrix} -E & 0 & 0 \\ 0 & 0 & 0 \\ 0 & 0 & 0 \end{pmatrix} \quad , \quad \dot{\mathbf{T}}_B = \begin{pmatrix} 0 & 0 & 0 \\ 0 & 0 & 0 \\ 0 & 0 & 0 \end{pmatrix}, \tag{9}$$

where at the point A, $\dot{\sigma}_1 = E\dot{\varepsilon}_1$ since $\dot{\sigma}_2 = 0$ and $\dot{\varepsilon}_1 = -1$.

Substituting $\mathbf{D}, \mathbf{T}$ and $\dot{\mathbf{T}}$ computed at points A and B into Eq. (4), the following system of equations is obtained with the unknowns C_1, C_2, C_3 and C_4:

[3] Because of the fluctuations in the simulation results the stress-strain curves cannot be differentiated easily. In order to obtain smooth curves, a fifth order polynomial has been fitted to the data and the slopes have been computed using the fitted curves.

$$\begin{pmatrix} \mathrm{tr}\mathbf{T}_A D^A_{1,1} & T^A_{1,1}\frac{\mathrm{tr}(\mathbf{TD})_A}{\mathrm{tr}\mathbf{T}_A} & ||\mathbf{D}_A||\frac{(T_{1,1})^2_A}{\mathrm{tr}\mathbf{T}_A} & ||\mathbf{D}_A||\frac{(T^*_{1,1})^2_A}{\mathrm{tr}\mathbf{T}_A} \\ \mathrm{tr}\mathbf{T}_A D^A_{2,2} & T^A_{2,2}\frac{\mathrm{tr}(\mathbf{TD})_A}{\mathrm{tr}\mathbf{T}_A} & ||\mathbf{D}_A||\frac{(T_{2,2})^2_A}{\mathrm{tr}\mathbf{T}_A} & ||\mathbf{D}_A||\frac{(T^*_{2,2})^2_A}{\mathrm{tr}\mathbf{T}_A} \\ \mathrm{tr}\mathbf{T}_B D^B_{1,1} & T^B_{1,1}\frac{\mathrm{tr}(\mathbf{TD})_B}{\mathrm{tr}\mathbf{T}_B} & ||\mathbf{D}_B||\frac{(T_{1,1})^2_B}{\mathrm{tr}\mathbf{T}_B} & ||\mathbf{D}_B||\frac{(T^*_{1,1})^2_B}{\mathrm{tr}\mathbf{T}_B} \\ \mathrm{tr}\mathbf{T}_B D^B_{2,2} & T^B_{2,2}\frac{\mathrm{tr}(\mathbf{TD})_B}{\mathrm{tr}\mathbf{T}_B} & ||\mathbf{D}_B||\frac{(T_{2,2})^2_B}{\mathrm{tr}\mathbf{T}_B} & ||\mathbf{D}_B||\frac{(T^*_{2,2})^2_B}{\mathrm{tr}\mathbf{T}_B} \end{pmatrix} \begin{pmatrix} C_1 \\ C_2 \\ C_3 \\ C_4 \end{pmatrix} = \begin{pmatrix} -E \\ 0 \\ 0 \\ 0 \end{pmatrix} \tag{10}$$

where for clarity the letters A and B have been switched to superscripts when the indicial notation of the tensors is used. The solution to (10) can be obtained by simple matrix inversion using linear algebra or well known numerical methods such as e.g. Gauss-Seidel.

References

1. D. Mueth, H. Jaeger, S. Nagel, Physical Review E **57**(3), 3164 (1998)
2. B. Miller, C. O'Hern, R. Behringer, Physical Review Letters **77**(15), 3110 (1996)
3. J.T. Jenkins, M. Satake (eds.), *Micromechanics of Granular Materials* (Elsevier, Amsterdam, 1988)
4. P.A. Cundall, O.D.L. Strack, Géotechnique **29**(1), 47 (1979)
5. S. Nemat-Nasser, Journal of the Mechanics and Physics of Solids **48**(6-7), 1541 (2000)
6. J. Christoffersen, M. Mehrabadi, S. Nemat-Nasser, Journal of Applied Mechanics **48**(2), 339 (1981)
7. M. Mehrabadi, B. Loret, S. Nemat-Nasser, Proceedings of the Royal Society A: Mathematical, Physical and Engineering Sciences **441**(1913), 433 (1993)
8. S. Luding, Granular Matter **10**(4), 235 (2008)
9. I. Agnolin, J.N. Roux, Physical Review E **76**(6), 1 (2007)
10. L. Silbert, D. Erta, G. Grest, T. Halsey, D. Levine, Physical Review E **65**(3), 51302 (2002)
11. T. Majmudar, M. Sperl, S. Luding, R. Behringer, Physical Review Letters **98**(5), 1 (2007)
12. C.S. OHern, L.E. Silbert, S.R. Nagel, Physical Review E **68**(1) (2003)
13. F. Göncü, O. Durán, S. Luding, Comptes Rendus Mécanique **338**(10-11), 570 (2010)
14. M.R. Shaebani, M. Madadi, S. Luding, D. Wolf, Physical Review E **85**(1), 11 (2012)
15. S. Luding, E. Bauer, in *Geomechanics and Geotechnics: From Micro to Macro, Vols 1 and 2*, ed. by M. Jiang, MJ and Liu, F and Bolton. Int Soc Soil Mech & Geotechn Engn (CRC PRESS-TAYLOR & FRANCIS GROUP, 6000 BROKEN SOUND PARKWAY NW, STE 300, BOCA RATON, FL 33487-2742 USA, 2011), pp. 495–499

16. S. Luding, Particulate Science and Technology **26**(1), 33 (2007)
17. H. Makse, D. Johnson, L. Schwartz, Physical Review Letters **84**(18), 4160 (2000)
18. V. Ogarko, S. Luding, The Journal of Chemical Physics **136**(12), 124508 (2012)
19. F. Göncü, O. Durán, S. Luding, in *Powders and Grains 2009: Proceedings of the 6th International Conference on Micromechanics of Granular Media, 13-17 July 2009, Golden, Colorado*, ed. by M. Nakagawa, S. Luding (AIP, 2009), pp. 531–534
20. D.C. Drucker, W. Prager, Quarterly of Applied mathematics **10**, 157 (1952)
21. A. Suiker, A. Metrikine, R. de Borst, International Journal of Solids and Structures **38**(9), 1563 (2001)
22. A.S.J. Suiker, R. de Borst, Philosophical transactions. Series A, Mathematical, physical, and engineering sciences **363**(1836), 2543 (2005)
23. D. Kolymbas, Archive of Applied Mechanics **61**, 143 (1991)
24. W. Wu, E. Bauer, D. Kolymbas, Mechanics of Materials **23**(1), 45 (1996)
25. D. Kolymbas, *Introduction to Hypoplasticity (Advances in Geotechnical Engineering and Tunneling)*, 1st edn. (A.A. Balkema, Rorrerdam, 1999)
26. O.I. Imole, N. Kumar, V. Magnanimo, S. Luding, KONA Powder and Particle Journal **30**, 84 (2013)
27. O. Durán, N. Kruyt, S. Luding, International Journal of Solids and Structures **47**(17), 2234 (2010)
28. O. Durán, N. Kruyt, S. Luding, International Journal of Solids and Structures **47**(2), 251 (2010)
29. A.N. Schofield, P. Wroth, *Critical state soil mechanics* (McGraw-Hill, 1968)
30. M. Oda, J. Konishi, S. Nemat-Nasser, Mechanics of Materials **1**(4), 269 (1982)
31. A.S.J. Suiker, N.A. Fleck, Journal of Applied Mechanics **71**(3), 350 (2004)
32. J. Bardet, Mechanics of Materials **18**(2), 159 (1994)
33. S. Antony, N. Kruyt, Physical Review E **79**(3), 31308 (2009)
34. R. Tykhoniuk, J. Tomas, S. Luding, M. Kappl, L. Heim, H.J. Butt, Chemical Engineering Science **62**(11), 2843 (2007)
35. K. Been, M.G. Jefferies, Géotechnique **35**(2), 99 (1985)
36. D. Kolymbas, W. Wu, Powder Technology **60**(2), 99 (1990)
37. S. Luding, E.S. Perdahcioglu, Chemie Ingenieur Technik **83**(5), 672 (2011)
38. V. Magnanimo, S. Luding, Granular Matter **13**(3), 225 (2011)